XLVI CILAMCE
VITÓRIA - ES - BRAZIL - 2025
XLVI IBERO-LATIN AMERICAN CONGRESS ON COMPUTATIONAL METHODS IN ENGENEERING

# Numerical study of non-spherical particle transport in a duct by Newtonian fluid using the lattice Boltzmann method

Joana L. Gemeli[1], Marco A. Ferrari[1], Admilson T. Franco[1]

[1]*Research Center for Rheology and Non-Newtonian Fluids (CERNN), Postgraduate Program in Mechanical and Materials Engineering, Federal University of Technology - Paraná (UTFPR)*
*Bloco N - R. Dep. Heitor Alencar Furtado, 5000 - Ecoville, 81280-340, Curitiba, Paraná, Brazil*
*joana.2001@alunos.utfpr.edu.br, e.marcoferrari@utfpr.edu.br, admilson@utfpr.edu.br*

**Abstract.** During the drilling process of petroleum wellbores, a bit tool uses a rotary motion combined with axial pressure to break the rock formation of the well walls into cuttings. The gravel needs removing; otherwise, it tends to pile up at the bottom of the well, and accumulated rocks can lead to prolonged execution times, increased pressure, and eventually render the well inoperative. The rock pieces extracted from the drilling process have complex geometries; therefore, groups of less complex particles, such as ellipsoidal particles, can model the granular material. Due to the high complexity of solving these flows with immersed particles, numerical simulations are powerful tools to assess the behavior of such flows. One method of studying the transport of particles is the coupling of the lattice Boltzmann method (LBM) and the immersed boundary method (IBM). The LBM employs a mesoscopic approach to describe the fluid as a population of particles evolving over time, where the Boltzmann equation governs the evolution, which contains a collision operator responsible for changes in the velocity and direction of the particles. The IBM uses the force density in the Navier-Stokes equation to mimic a boundary condition, its basis is a two-node system, where an Eulerian grid defined by the LBM is stationary, and the IBM marker points are Lagrangian nodes that are not bound to the Eulerian grid and can move freely. The main goal of this work is to assess the influence of the velocity, through the Reynolds number, on the cleaning of petroleum wellbores. To analyze this phenomenon, we evaluated the transport of 40 prolate particles in a duct filled with glycerin (4 °C). The density ratio was 2.14, the particles' aspect ratio was 2, a geometric mean radius of 25 mm, and their diameter ratio to the duct diameter was 1:10. In the Reynolds range analyzed, from 100 to 250, we observed that in some cases, there was a negative particle mass transport rate (the particles settle faster than they can be transported), passing through zero, and then, for higher Reynolds numbers, presenting a positive mass transport rate.

**Keywords:** LBM, IBM, Prolate particle, Duct, Transport rate.

## 1 Introduction

Transporting liquid and solid particles through a duct is critical in the gas and petroleum industry [1]. During the exploration process of rock formation on the seabed, such as the pre-salt, a drilling bit attached to a rotating pipe excavates the wellbore [2]. In the process, cuttings are detached from the rock wall, and the continuous removal of particles from the wellbore is essential. Preventing blockades, promoting uninterrupted petroleum flow, and prolonging the lifespan of both tools and the well are essential goals of the process [3].

Many present-day CFD techniques, such as finite volumes and finite elements, depend heavily on high computational times and resource requirements, leading to limited domain sizes [1]. Combined with computational techniques for particulate flows, e.g., discrete element method (DEM) and other particle-based methods such as smoothed particle hydrodynamics (SPH), particle-in-cell (PIC), and material point method (MPM), which all require a careful calibration process [4], leads to a barrier to their use as industrial tools.

The lattice Boltzmann method emerges as a mechanism that combines a mesoscopic scale and a high parallelization possibility, dropping simulation times [5], and when coupled with the immersed boundary method, which utilizes a two-grid system that allows particles to move freely, independent of the LBM grid [6], enables large domains, large amounts of arbitrarily shaped particles, and a fair range of flow parameters, outperforming the traditional tools [7].

Although most works focus on spherical particles, the study of non-spherical particles remains less explored

due to the lack of analytical solutions and the difficulty in determining shape, contact points, and complex force models. However, the industrial application presented above could benefit from studies with non-spherical gravel. Therefore, this work presents a simulation of 40 prolate particles in a pipe, evaluating how different velocities influence the cleaning of the duct.

## 2 Numerical method

### 2.1 Lattice Boltzmann method

The lattice Boltzmann method (LBM) works by considering a mesoscopic scale population of fluid particles that behave according to the Boltzmann equation. The collision term is a function that gives the net balance between molecules that acquire a certain velocity and those that lose this velocity. In equilibrium conditions, this balance must be null; otherwise, the distribution would vary over time and space. It is possible to obtain the Maxwell-Boltzmann equilibrium distribution through the collision invariants and moments of equilibrium.

A model capable of recovering the main properties of the original collision operator makes the jump from the Boltzmann equation to the LBM. Bhatnagar et al. [8] proposed a simplification of the operator, denominated the BGK collision operator, defined as:

$$\Omega_i = \frac{\bar{f}_i^{eq} - \bar{f}_i}{\tau^*}, \tag{1}$$

where a relaxation term replaces the collision term with a single relaxation time, $\tau^*$, $\bar{f}_i^{eq}$ and $\bar{f}_i$ are the discrete equilibrium population and dimensionless populations, respectively.

For the discretization of the Boltzmann equation, it is necessary to substitute not only the continuum physical space, representing $\mathbf{x}$ for points $\mathbf{x}_i$, but also the velocity field, representing $\boldsymbol{\xi}$ as velocity vectors $\boldsymbol{\xi}_i$, enabling the evaluation of $f$ at different times separated by time steps. Replaced by a dimensionless version, the discretized Boltzmann equation relates the molecular velocity to the lattice vectors, $\mathbf{e}_i$, through the lattice speed, $c$. Thus, the discretized in velocity space and dimensionless Boltzmann equation with a force term, $\bar{F}_i$, becomes:

$$\partial_t \bar{f}_i + e_{i\alpha}\partial_\alpha \bar{f}_i = \bar{\Omega}_i + \bar{F}_i. \tag{2}$$

In time $t+1$, the particle population along the direction $i$ in the point $\mathbf{x} + \Delta\mathbf{x}$ can be found through a second-order Taylor series expansion, where the physical space and the velocity field are joined by $\Delta\mathbf{x} = \mathbf{e}_i h$, where $h$ is the orthogonal distance between two adjacent sites. The resulting equation is implicit, but with a variable change proposed by He et al. [9], the LBE becomes:

$$\bar{f}_i(\mathbf{x} + \mathbf{e}_i h, t+1) = \bar{f}_i(\mathbf{x}, t) + \frac{\bar{f}^{eq} - \bar{f}_i}{\tau} + \left(1 - \frac{1}{2\tau}\right)\bar{F}_i(\mathbf{x}, t), \tag{3}$$

where $\bar{f}_i$ is the modified distribution and $\tau = \tau^* + 1/2$.

Finally, the discretized equilibrium function, obtained by Hermite polynomial expansions:

$$\bar{f}_i^{eq} = w_i \rho_f \left[1 + \frac{c_{i\alpha}u_\alpha}{c_s^2} + \frac{u_\alpha u_\beta (c_{i\alpha}c_{i\beta} - c_s^2\delta_{\alpha\beta})}{2c_s^4}\right], \tag{4}$$

where $\rho_f$ is the fluid density, $c_s$ is the speed of sound, which for the $D3Q19$ velocity set, chosen in this work is equivalent to $1/\sqrt{3}$, $u$ is the fluid velocity, $c_i$ is the velocity vector, and $w_i$ is the directional weight, which for $D3Q19$ are: for $i = 0$ is $12/36$, from $i = 1$ to 6 is $2/36$ and for $i = 7$ to 18 is $1/36$.

Since knowing the particle populations is not enough to solve problems, one can obtain the macroscopic properties: pressure and velocity, through the fact that the LBM preserves the macroscopic moments according to:

$$\rho_f = \sum_i \bar{f}_i, \tag{5a}$$

$$\rho_f u_\gamma = \sum_i \bar{f}_i e_{i\gamma} + \frac{1}{2}\sum_i \bar{F}_i e_{i\gamma}. \tag{5b}$$

A framework that allows for the correct retrieval of the macroscopic equations from the LBE is the Chapman-Enskog method, thoroughly described by Chapman and Cowling [10]. The technique relies on the idea that a gas is close to equilibrium, with small deviations. By assuming these deviations are minor, the method expands the particle distribution function in terms of a small parameter, typically related to the Knudsen number, and

systematically solves for each level of approximation. At first order in the Knudsen number, one can derive the Navier-Stokes equations:

$$\partial_t \rho_f + \partial_\alpha(\rho_f u_\alpha) = 0; \tag{6a}$$
$$\partial_t(\rho_f u_\beta) + \partial_\alpha(\rho_f u_\alpha u_\beta + P\delta_{\alpha\beta}) = -\partial_\alpha \sigma_{\alpha\beta}, \tag{6b}$$

where $P$ is the pressure and $\sigma_{\alpha\beta}$ is the viscous stress tensor, which is given by:

$$\sigma_{\alpha\beta} = -\mu_1(\partial_\alpha u_\beta + \partial_\beta u_\alpha) + \mu_2 \partial_\alpha u_\beta \delta_{\alpha\beta}, \tag{7}$$

where $\mu_1$ and $\mu_2$ are, respectively, the shear viscosity and the volumetric viscosity, given by:

$$\mu_1 = \rho_f c_s^2(\tau - 1/2); \tag{8a}$$
$$\mu_2 = (2/D)\mu_1, \tag{8b}$$

where $D$ is the number of Euclidean dimensions. To construct the boundary conditions required for modeling the duct walls, we employed the interpolated bounce-back method proposed by Bouzidi et al. [11], assuming that $\mathbf{r}_l$ is a fluid node and $\mathbf{r}_l + \mathbf{c}_i$ is a solid node. Letting $\mathbf{c}_i'$ be the reverse velocity of $\mathbf{c}_i$, where $\mathbf{c}_i' = -\mathbf{c}_i$. Through linear interpolation:

$$f_{i'}(\mathbf{r}_l, t+1) = 2q f_i^c(\mathbf{r}_l, t) + (1-2q) f_i^c(\mathbf{r}_l - \mathbf{c}_i, t), q < 1/2; \tag{9a}$$
$$f_{i'}(\mathbf{r}_l, t+1) = \frac{1}{2q} f_i^c(\mathbf{r}_l, t) + \frac{(2q-1)}{2q} f_{i'}^c(\mathbf{r}_i, t), q \geq 1/2, \tag{9b}$$

where if we take $A$ as the last fluid node and $B$ as the first solid node, with the wall between them at $C$, $q$ is given by $|AC|/|AB|$. On the RHS, $f^c$ are taken after collision and before propagation, and at the LHS, $f_{i'}(\mathbf{r}_l, t+1)$ will be used at values after collision and after propagation, after a complete time step.

### 2.2 Immersed boundary method

Peskin [6] developed the immersed boundary method to study blood flow dynamics within a heart. The method works by introducing a body force term to the momentum transport equations to account for the presence of the immersed body, calculating the direction and magnitude of the force in such a way as to reproduce the effects of the body immersed in the flow. The IBM uses Lagrangian points with the same velocity as the fluid to guarantee a non-slip condition at the surface.

Peskin [12] noted that the force is infinite at the surface and null everywhere else, which would cause problems in discretization. Replacing the Dirac function addresses the issue with a diffuse approximation for the non-slip condition:

$$\varrho(\mathbf{x} - \mathbf{X}(s,t)) = \frac{1}{h^3}\phi\left(\frac{\Delta x}{h}\right)\phi\left(\frac{\Delta y}{h}\right)\phi\left(\frac{\Delta z}{h}\right), \tag{10}$$

where $\Delta x$, $\Delta y$, and $\Delta z$ are the Cartesian distances between Lagrangian nodes and Eulerian lattices, $\phi$ is the kernel function responsible for said diffusion. One of the kernel functions proposed by Peskin [12], which met all the required postulates:

$$\phi_4(r) = \begin{cases} \frac{1}{8}\left(3 - 2|r| + \sqrt{1 + 4|r| - 4|r|^2}\right) & 0 \leq |r| \leq 1; \\ \frac{1}{8}\left(5 - 2|r| - \sqrt{-7 + 12|r| - 4|r|^2}\right) & 1 < |r| \leq 2; \\ 0 & 2 < |r|, \end{cases} \tag{11}$$

where $r$ is the distance between the Lagrangian node and the Eulerian lattice. The $\phi_4$ has a smooth distribution that affects 16 lattices in 2D and 64 in 3D.

From the definition of the Eulerian (fluid) velocity, one may decompose it into two terms: a force-free velocity, $\mathbf{u}^{E,noF}$, and a discrete force correlation term, $\mathbf{F}^L$. After some algebraic manipulation, the resulting discrete equation is:

$$\mathbf{u}^L = \sum_E \mathbf{u}^{E,noF} \varrho(\mathbf{x}-\mathbf{X}) h^3 + \sum_E \left[ \sum_L \frac{\Delta t}{2\rho_f} \mathbf{F}^L \varrho(\mathbf{x}-\mathbf{X}) \Delta S \right] \varrho(\mathbf{x}-\mathbf{X}) h^3, \tag{12}$$

where $\Delta S$ is the surface area of the Lagrangian node.

One could solve the resulting linear system via matrix inversion, but this would limit the domain sizes. Ayala et al. [13] proposed an iterative method to bypass this procedure. The process follows these steps: after the LBM streaming step, the algorithm calculates the uncorrected velocities without including the IBM force. It then computes the unforced velocity at the Lagrangian node, where the iterative process begins with sub-step $m$. In the first step, the algorithm evaluates the force on the boundary node as:

$$\mathbf{F}^{L,m+1} = 2\rho_f \frac{\mathbf{u}^{L,m} - \sum_E \mathbf{u}^{E,m} \varrho(\mathbf{x}-\mathbf{X}) h^3}{\Delta t}, \tag{13}$$

next, it distributes the force to the Eulerian lattices, evaluates the fluid velocities with the force correction term, and recalculates the velocity boundary condition node. The algorithm returns to Eq. 12 and repeats the process. In the case studied here, one iteration ensured the non-slip condition. Finally, the algorithm applies the necessary force to the Eulerian lattices to change the fluid state from one where the immersed body does not exist to one where it does.

Besides the particle boundaries, modeling their dynamics is essential. The forces calculated above act on the particles, which are subject to Newton's second law. Adding the contact forces and torques due to collision, $\mathbf{F}_c$, and $\mathbf{T}_c$, Newton's second law becomes:

$$m_p \frac{d\mathbf{u}_p}{dt} = \iint_S \boldsymbol{\sigma} \cdot d\mathbf{s} + (\rho_p - \rho_f) \mathcal{V}_p \mathbf{g} + \mathbf{F}_c; \tag{14a}$$

$$\mathbf{I}_p \frac{d\boldsymbol{\omega}_p}{dt} = \iint_S \mathbf{r} \times (\boldsymbol{\sigma} \cdot d\mathbf{s}) + \mathbf{T}_c, \tag{14b}$$

where $m_p$, $\mathbf{u}_p$ and $\mathcal{V}_p$ are the particle mass, velocity, and volume, respectively, and $\boldsymbol{\sigma} \cdot d\mathbf{s}$ is the force acting at the particle's surface. $\mathbf{I}_p$, $\boldsymbol{\omega}_p$, are the particle moment of inertia and angular velocity, $\mathbf{r}$ is the distance from the center of mass to the particle surface, and $d\mathbf{s}$ is an infinitesimal element of the particle's surface.

The method chosen to discretize the equations Eq. 14a and Eq. 14b was a semi-implicit Runge-Kutta defined by Ardekani et al. [14]:

$$\mathbf{u}_p^t = \mathbf{u}_p^{t-1} - \frac{1}{\mathcal{V}_p} \frac{\rho_f}{\rho_p} \sum_{s \in \mathbf{P}} \mathcal{F}^{t-1/2} \Delta S + \left(1 - \frac{\rho_f}{\rho_p}\right) \mathbf{g} + \frac{1}{\rho_p \mathcal{V}_p} \frac{\mathbf{F}_c^t - \mathbf{F}_c^{t-1}}{2}; \tag{15a}$$

$$\mathbf{I}_p^t \, \boldsymbol{\omega}_p^t = \mathbf{I}_p^{t-1} \, \boldsymbol{\omega}_p^{t-1} - \rho_f \sum_{s \in \mathbf{P}} \mathbf{x}^{t-1} \times \mathcal{F}^{t-1/2} \Delta S + \frac{\mathbf{T}_c^t - \mathbf{T}_c^{t-1}}{2}, \tag{15b}$$

where Eq. 15a is the translation component of the particle, and Eq. 15b is the rotational component. $\mathcal{F}$ is the force density.

## 3 Validations

We conducted the validation process for the implemented numerical method to independently test each added complexity of the problem. Firstly, to test the LBM $D3Q19$ velocity set, we simulated a pressure-driven laminar flow between parallel plates. Then, for the IBM and particle dynamics, we performed a sedimentation experiment of a single particle in a closed domain. Lastly, we conducted a rotation of a prolate particle in a simple shear flow to test the accuracy of the non-spherical particles model.

***Parallel Plates***: The simulation was run in a cubic domain with a boundary condition of parallel plates with bounce back, positioned at $y = 0$ and $y = 1$, and compared to the analytical normalized equation:

$$u_{ref}(z) = 6(z - z^2), \tag{16}$$

where $u_{ref}$ is the velocity normalized by the mean velocity and $z$ is the distance normalized by the channel length. Four tests were conducted to compare the obtained errors for each; the Reynolds number, $Re = 10$, the channel length, $L = 1$, and the relaxation time, $\tau = 0.62$, were kept the same, and the dimensional resolution was refined according to Tab. 1:

Table 1. Parameters for the simulation.

| $Case$ | $N_x \times N_y \times N_z$ | $u_f$ [l.u.][1] | $g$ [l.u.] |
|---|---|---|---|
| 1 | $8 \times 8 \times 8$ | 0.05 | $2.50 \times 10^{-4}$ |
| 2 | $16 \times 16 \times 16$ | 0.025 | $3.13 \times 10^{-5}$ |
| 3 | $32 \times 32 \times 32$ | 0.0125 | $3.91 \times 10^{-6}$ |
| 4 | $64 \times 64 \times 64$ | 0.00625 | $4.88 \times 10^{-7}$ |

[1] l.u. = lattice units.

We measured the deviation from the analytical results in terms of the quadratic error norm, $L_2$:

$$L_2 = \sqrt{\frac{\sum(u_{num} - u_{ref})^2}{\sum(u_{ref})^2}}, \tag{17}$$

where $u_{num}$ is the simulation obtained velocity and $u_{ref}$ is the value obtained from Eq. 16. One may use the $L_2$ to assess the truncation error of the numerical model. In Fig. 1 we observe a second-order behavior, confirming the method's spatial second-order accuracy for incompressible, laminar flow in a parallel plate geometry, attesting the correct implementation of the LBM $D3Q19$ velocity set.

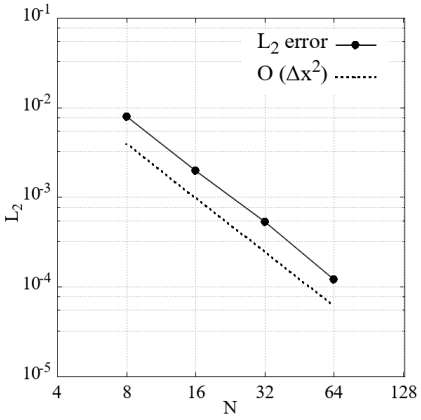



Figure 1. Quadratic error norm $L_2$ of the parallel plates validation for the D3Q19 velocity set. The dashed line shows the second-order truncation error.

***Sedimentation***: We tested the dynamic behavior of the IBM via the simulation of a spherical particle settling in a quiescent Newtonian fluid and compared it against the experimental work of Cate et al. [15]. The parameter evaluated was the terminal velocity for four cases with Reynolds numbers varying from 1.5 to 32 in the geometry shown in Fig. 2.

The particle had a diameter of 15 mm, a density of 1120 kg.m$^{-3}$, and was positioned three-quarters of the way inside a box domain of dimensions 100 mm $\times$ 100 mm $\times$ 160 mm and filled with Newtonian fluid. The three lattice refinements tested were: 1 mm, 0.66 mm, and 0.5 mm. Since the objective was to simulate an experimental work, the fluid properties varied, thus Tab. 2 contains the fluid properties and essential parameters for the LBM simulation for the lattice size 1 mm.

Figure 3 presents the results for this validation case. The graph shows the particle velocity as a function of time for the three refinements and the original work by Cate et al. [15]. As the mesh of simulations became more refined, the results converged closer to the experimental data, demonstrating the model's capacity to predict particle dynamics.

***Non-spherical particle in shear flow***: Lastly, we placed a prolate particle at the center of a creeping Couette flow between parallel plates with velocity in opposite directions to analyze its periodic rotation. Jeffery [16] derived an analytical solution for the angular velocity evolution of a non-spherical particle in an inertialess regime:

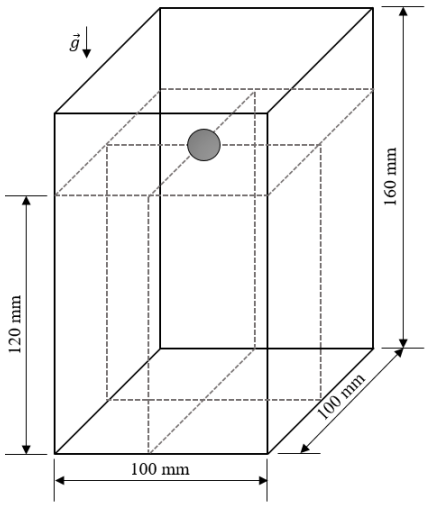



Figure 2. Geometry used in the work by Cate et al. [15] to simulate the sedimentation of a single spherical particle.

Table 2. Parameters for the simulation.

| $Case$ | $Re$ | $\rho_f$ [kg.m$^{-3}$] | $\mu_f$ [Pa.s] | $\tau$ | $g$ [l.u.] | $C_t$ [l.u.] |
|---|---|---|---|---|---|---|
| 1 | 1.5 | 970 | 0.373 | 0.90 | $1.18 \times 10^{-3}$ | $3.47 \times 10^{-4}$ |
| 2 | 4.1 | 965 | 0.212 | 0.90 | $3.61 \times 10^{-3}$ | $6.07 \times 10^{-4}$ |
| 3 | 11.6 | 962 | 0.113 | 0.80 | $7.11 \times 10^{-3}$ | $8.51 \times 10^{-4}$ |
| 4 | 31.9 | 960 | 0.058 | 0.65 | $6.72 \times 10^{-3}$ | $8.28 \times 10^{-4}$ |

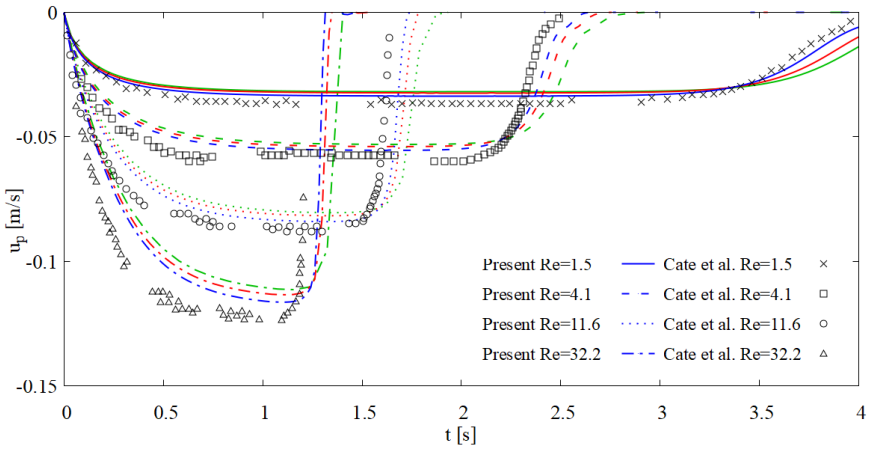



Figure 3. Particle settling velocity against the experimental work by Cate et al. [15] as a function of time for four Reynolds numbers, defined by the line type. Each line colors represents a different mesh: green for $\Delta x = 1$ mm, red for $\Delta x = 0.66$ mm, and blue for $\Delta x = 0.5$ mm.

$$\omega_p = -\frac{G}{a^2 + b^2}(a^2 sen^2\theta + b^2 cos^2\theta), \tag{18}$$

where $G$ is the imposed shear rate, $a$ and $b$ are the polar and equatorial semi-axes of the ellipsoidal particle. In this simulation, a neutrally buoyant particle with aspect ratio, $AR = b/a$, of 2 in a Couette flow of Reynolds 1.395 defined by shear rate, $G$, and an equivalent diameter, $D_{eq}$:

$$D_{eq} = 2(ab^2)^{1/3}, \tag{19}$$

was set in a domain of $256 \times 256 \times 512$ lattices, with $u_{wall} = 0.05$ and $\tau = 1.70$. The initial orientation of the particle was $\theta = 0$ with no initial angular velocity. Figure 3 shows the result, which presents great agreement with the analytical solution given by Eq. 18.

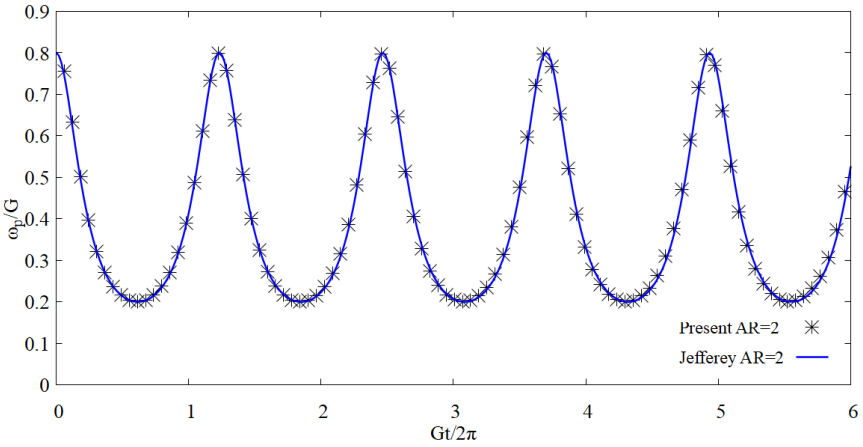



Figure 4. Angular velocity of the particle with $AR = 2$ against the analytical solution proposed by Jeffery [16]. Time becomes dimensionless by $G/2\pi$ and angular velocity by $G$.

The satisfactory validation of the LBM, the IBM, and non-spherical particle dynamics provides a solid foundation to advance our analysis of the velocity influence in particle transport inside a duct.

## 4 Results

Drilling an oil wellbore typically involves creating a hole ranging from 6 to 10 inches in diameter. The process begins with a surface hole, drilled using a rotary drilling rig and a drill bit mounted on a long string of pipes. The operation requires drilling fluid circulation to cool the bit, carry rock cuttings to the surface, and stabilize the wellbore.

We simulated this process using a domain representing a tube with a diameter of 256 mm and a length of 512 mm, applying periodic boundary conditions to emulate an infinitely long tube. Forty oblate particles of 25 mm of equivalent diameter were evenly spaced within the tube. The fluid chosen to carry the rock particles was glycerin at 4 °C, with a density, $\rho_f$, of 1260 kg.m$^{-3}$ and a dynamic viscosity, $\mu_f$, of 1.84 Pa.s, and the gravel particles have a density, $\rho_p$, of 2700 kg.m$^{-3}$, resulting in a density ratio of $\rho_p/\rho_f = 2.14$. Figure 4 shows a schematic representation of the problem.

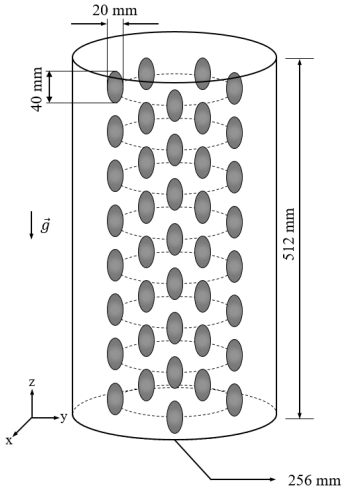



Figure 5. Visual representation of the domain geometry used to simulate the problem.

The conversion parameter for distances, $C_x$, used to calculate the LBM dimensions was $1 \times 10^{-3}$. It resulted in a tube with a diameter of 256 l.u. and a length 512 l.u. Forty particles with polar axis equal to 40 l.u. and equatorial axis of 20 l.u. were placed in rings of five evenly spaced particles, in eight rows 66 l.u. apart from each other and 25 l.u. from the edge of the domain. The lattice velocity, $u_f$, was 0.1, and Tab. 3 shows the other essential parameters. Based on the Hagen-Poiseuille parabolic velocity profile, we calculated the force, $F_z$:

$$F_z = \frac{4u_f\mu_1}{(D_{duct}/2)^2}, \tag{20}$$

where $D_{duct}$ is the duct diameter and $\mu_1$ is the shear viscosity defined in Eq. 8a. The Reynolds numbers, defined as:

$$Re = \frac{\rho_f u_f D_{duct}}{\mu_1}, \tag{21}$$

had the values: 100, 150, 200, and 250.

Table 3. Parameters for the simulation.

| $Case$ | $Re$ | $\tau$ | $g$ [l.u.] | $F_z$ [l.u.] |
|---|---|---|---|---|
| 1 | 100 | 1.268 | $3.01 \times 10^{-4}$ | $6.25 \times 10^{-6}$ |
| 2 | 150 | 1.012 | $1.34 \times 10^{-4}$ | $4.17 \times 10^{-6}$ |
| 3 | 200 | 0.884 | $7.54 \times 10^{-5}$ | $3.13 \times 10^{-6}$ |
| 4 | 250 | 0.8072 | $4.82 \times 10^{-5}$ | $2.50 \times 10^{-6}$ |

Figure 6 presents the results of the average velocity of the particles, $u_p$, over the time. We observe that the average velocity for the lowest Reynolds, 100, was below zero throughout the simulation, meaning that the fluid velocity was not sufficient to transport the particles out of the domain. After an increase, at $Re = 150$, the average velocity increased, and it is possible to observe the value fluctuating around zero, indicating that this Reynolds number represents the case of zero mass flux.

The first Reynolds number at which the particles could be carried across the zero average velocity was $Re = 200$. Around the 1.5-second mark, the particles began to rise instead of falling. Lastly, for the greatest Reynolds number, before the 1-second mark, the flow is strong enough to transport all the particles upward and accelerate them even more than $Re = 200$.

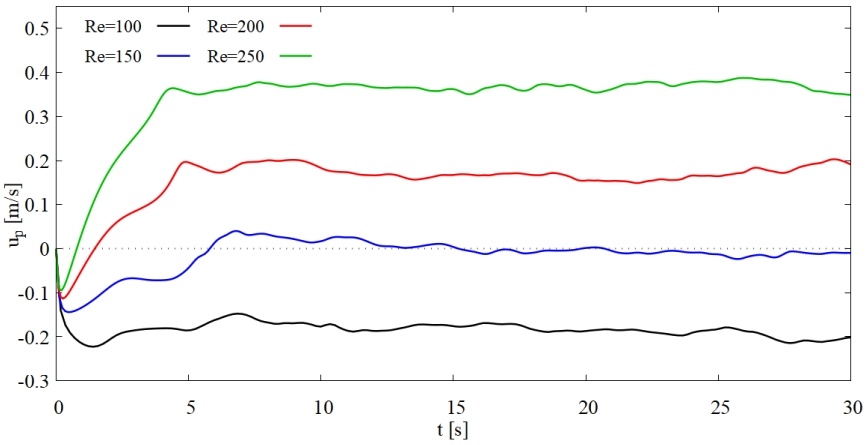



Figure 6. Average velocity of the particles over time for the four Reynolds numbers tested in the present work.

Figure 7 represents the average of the *z-direction* dimensionless velocity, illustrating the behavior of the overall flow. At lower Reynolds numbers, $Re = 100$ and 150, the velocity distribution remains irregular and more strongly influenced by viscous forces and particle interactions, which hinders effective axial transport. Notably, at $Re = 150$, the net mass flux is approximately zero, indicating that the flow cannot transport enough particles to establish a net positive movement in the *z-direction*. This result suggests a critical threshold below which the suspension fails to maintain forward transport.

Higher Reynolds numbers correspond to increased inertial effects, leading to smoother and more stratified velocity profiles. As the Reynolds number increases, $Re = 200$ and 250, the velocity field becomes increasingly uniform, boundary layer effects become more localized, and the fluid's capacity to carry particles improves.

Figure 8 shows how the particle distribution evolved in the four simulations. Each color identifies a particle index. To enhance visualization, the analysis focused on the time interval from 1s to 5s, where Fig. 6 indicated the most pronounced particle motion. The fluid flowed upward through the duct, and the particles showed greater resistance to settling as the Reynolds number increased. After 1s, the first row, represented by light-yellow particles,

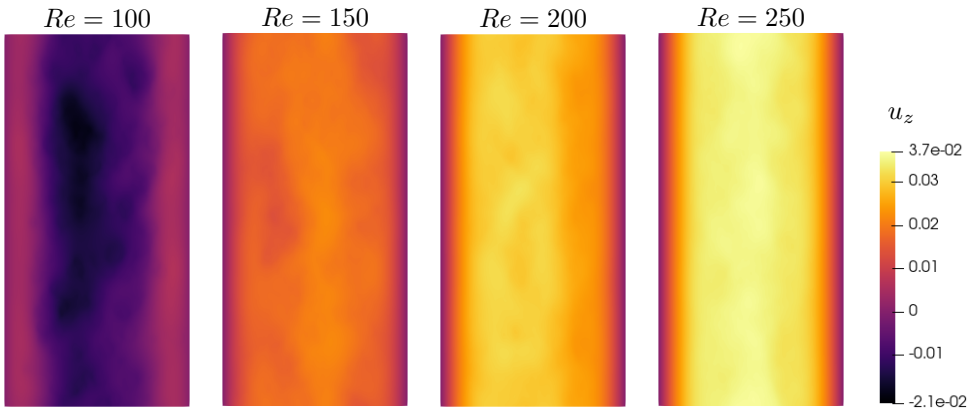



Figure 7. Representative image of the average dimensionless velocity in the *z-direction* obtained in the present work.

reached approximately halfway up the duct for $Re = 100$ and remained near the top for $Re = 250$. This result indicates that, although all particles initially settled at the beginning of the simulation, higher Reynolds numbers reduced the tendency to settle. By 5s, the particles for $Re = 100$ and 150 continued settling, while those for $Re = 200$ and 250 began to rise with the fluid flow. By the mark of 10s, all four cases exhibited complete particle mixing, and the simulations extended to 30s to confirm the steady-state condition.

## 5 Conclusions

The results show that at lower Reynolds numbers, $Re = 100$ and $Re = 150$, the fluid flow lacks sufficient inertia to sustain particle transport, resulting in a negative particle mass flux. It also indicates that the flow is not strong enough to suspend and carry the solid phase, leading to particle settling. In particular, the case of $Re = 150$ marks a critical point where the net mass flux is approximately zero, signifying a transitional regime between settling and transport. In contrast, for higher Reynolds numbers, $Re = 200$ and $Re = 250$, the increased flow velocity enhances inertial effects, allowing the fluid to overcome viscous and gravitational forces, thereby achieving a more positive and uniform particle mass transport.

**Acknowledgments.** The authors acknowledge the financial support of the Brazilian Coordination for the Improvement of Higher Education Personnel (CAPES), Finance Code 001.

**Authorship statement.** The authors hereby confirm that they are the sole liable persons responsible for the authorship of this work, and that all material that has been herein included as part of the present paper is either the property (and authorship) of the authors, or has the permission of the owners to be included here.

## References

[1] Z. Xu, K. Shen, J. Zhou, Q. Huang, P. Liu, J. Du, and J. Wu. Chemical sand production control: a review of materials, methods and characterization, 2024.

[2] B. Pang, X. Ren, Z. Liu, X. Wang, and X. Liu. Investigation on multiphase flow of multi-size cuttings particles and non-Newtonian drilling fluids in oil and gas horizontal well drilling using kinetic theory of granular flow. *Energy*, vol. 282, 2023.

[3] J. J. Casarin. *Investigação numérica do escoamento líquido-sólido de fluido viscoplástico em seção anular rotativa.* PhD thesis, Universidade Técnologica Federal do Paraná, 2021.

[4] C. R. Windows-Yule and A. Neveu. Calibration of dem simulations for dynamic particulate systems. *Papers in Physics*, vol. 14, 2022.

[5] A. Randles and E. Kaxiras. Parallel in time approximation of the lattice Boltzmann method for laminar flows. *Journal of Computational Physics*, vol. 270, pp. 577–586, 2014.

[6] C. S. Peskin. Flow patterns around heart valves: A numerical method, 1972.

[7] A. Stanier and L. Chacón. A conservative implicit-PIC scheme for the hybrid kinetic-ion fluid-electron plasma model on curvilinear meshes. *Journal of Computational Physics*, vol. 459, 2022.

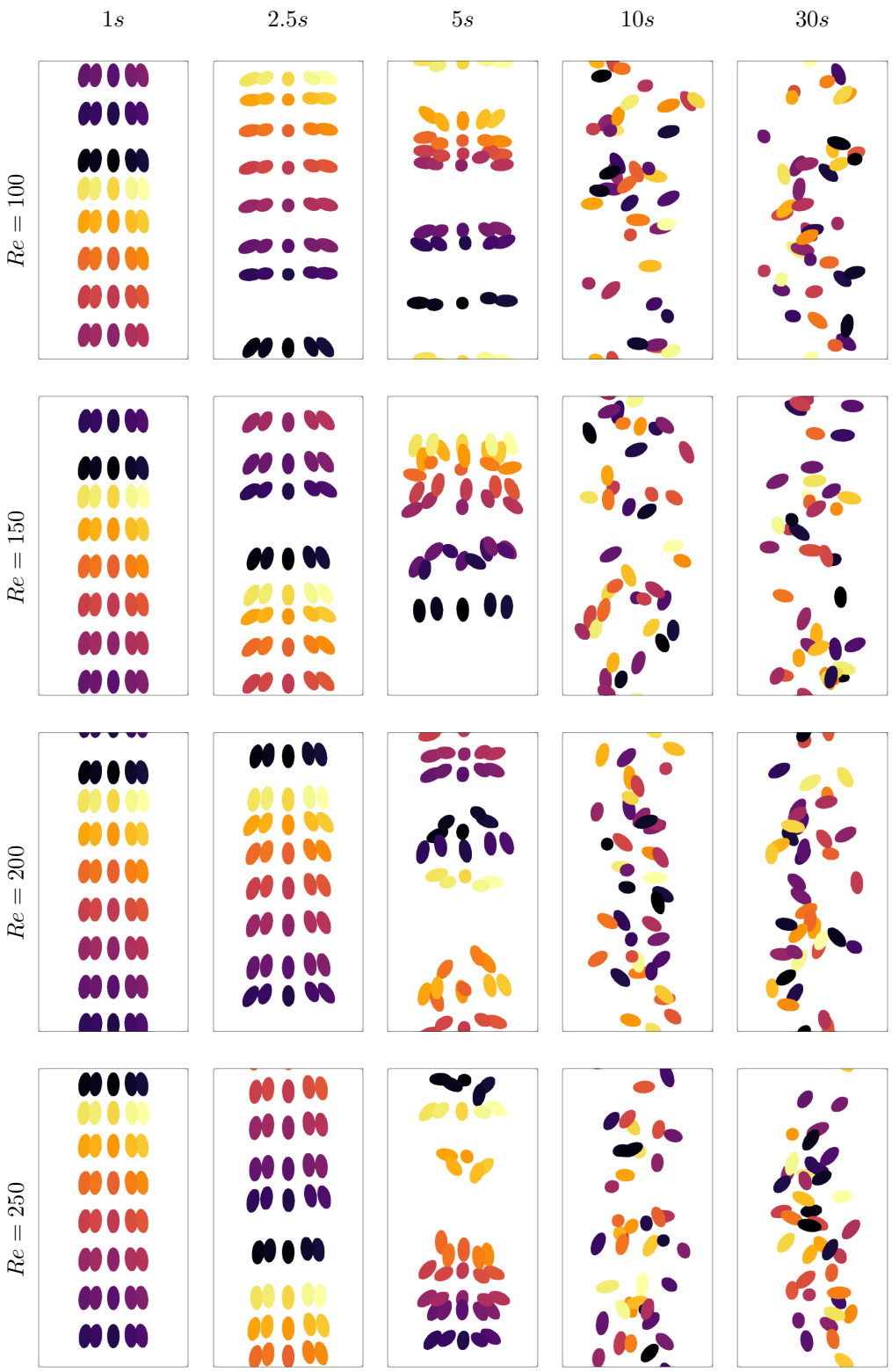



Figure 8. Representative image of the particles over time for the four cases obtained in the present work, the colors represent the particle index.

[8] P. L. Bhatnagar, E. P. Gross, , and M. Krook. A model for collision processes in gases. I. Small amplitude processes in charged and neutral one-component systems. *Physical Review*, vol. 94, 1954.
[9] X. He, S. Chen, and G. D. Doolen. A novel thermal model for the lattice Boltzmann method in incompressible limit, 1998.
[10] S. Chapman and T. G. Cowling. *The mathematical theory of non-uniform gases: an account of the kinetic theory of viscosity, thermal conduction and diffusion in gases*. Cambridge University Press, 1990.

[11] M. Bouzidi, M. Firdaouss, and P. Lallemand. Momentum transfer of a Boltzmann-lattice fluid with boundaries. *Physics of Fluids*, vol. 13, pp. 3452–3459, 2001.
[12] C. S. Peskin. The immersed boundary method. *Acta Numerica*, vol. 11, pp. 479–517, 2002.
[13] O. M. Ayala, L.-P. Wang, C. Peng, and O. M. Ayala. A comparative study of immersed boundary method and interpolated bounce-back scheme for no-slip boundary treatment in the lattice Boltzmann method: Part I, laminar flows. *International Journal for Numerical Methods in Fluids*, vol. 66, 2011.
[14] M. N. Ardekani, P. Costa, W. P. Breugem, and L. Brandt. Numerical study of the sedimentation of spheroidal particles. *International Journal of Multiphase Flow*, vol. 87, pp. 16–34, 2016.
[15] A. T. Cate, C. H. Nieuwstad, J. J. Derksen, and den H. E. V. Akker. Particle imaging velocimetry experiments and lattice-Boltzmann simulations on a single sphere settling under gravity. *Physics of Fluids*, vol. 14, pp. 4012–4025, 2002.
[16] G. B. Jeffery. The motion of ellipsoidal particles immersed in a viscous fluid, 1922.